Design and experimental characterization of a small flexible TMR-based indentation probe for soft tissue hardness estimation

Giacomo Santona[1], Antonio Fiorentino[2], Francesco Doglietto[3,4] and Mauro Serpelloni[1,*]

[1] Department of Information Engineering, Universit`a degli Studi di Brescia, Via Branze 38, 25123 Brescia, Italy
[2] Department of Mechanical and Industrial Engineering, Universit`a degli Studi di Brescia, Via Branze 38, 25123 Brescia, Italy
[3] Neurosurgery, Department of Neurosciences, Sensory Organs and Thorax, Largo Agostino Gemelli, 8, 00168 Rome, Italy
[4] Neurosurgery, Fondazione Policlinico Universitario A. Gemelli IRCCS, Largo Agostino Gemelli, 8, 00168 Rome, Italy

E-mail: mauro.serpelloni@unibs.it, giacomo.santona@unibs.it, antonio.fiorentino@unibs.it and francesco.doglietto@unicatt.it

Abstract

The endoscopic transsphenoidal approach is a surgical method used to remove pituitary adenomas—benign tumors located near the pituitary gland. The success of this procedure depends heavily on assessing the tumor's consistency, which is currently based on the surgeon's tactile feedback and experience. This study presents the development of a novel sensor-based probe designed to provide real-time measurements of tissue hardness, supporting more objective surgical decision-making. The probe integrates a tunneling magneto resistance (TMR) sensor with a deformable, 3D-printed tip made of thermoplastic polyurethane. The tip features micro-beams that deform upon contact with tissue; the extent of deformation, measured by the TMR sensor, correlates with tissue stiffness. The flexible structure was fabricated using fused filament fabrication, and the process was characterized to control micro-beam dimensions by adjusting print parameters such as layer height, print speed, and nominal line width. A regression model was developed to predict beam width with high accuracy and repeatability. Eighteen probe designs, combining different beam widths (0.42 mm–0.63 mm) and numbers (3–5), were tested through indentation experiments on samples with Shore 000 hardness ranging from 51 to 83 (ASTM D2240), including a cooked egg white sample as a biological tissue analogue. Results revealed that probes with 4 and 5 beams printed at lower speeds offered superior sensitivity, linearity, and uniformity. In these configurations, the probe was able to estimate the hardness of adenoma-like materials with errors below 2%. These findings validate the proposed system's potential for clinical use in evaluating soft to moderately firm tumors during surgery.

Keywords: mini tissue probe, TMR sensor, pituitary adenoma hardness, 3D printing, shore 000 hardness scale, measurement instruments

1. Introduction

The pituitary adenoma (PA) is a tumor, usually benign, that affects the pituitary gland [1, 2]. The gland is in the sella turcica, a saddle-shaped region on the back of the sphenoid bone, in the middle of the skull base. The tumor is surrounded by delicate anatomical structures such as the optic chiasm, the internal carotid artery or the arachnoid membrane, therefore it needs to be treated. The dimensions of the PA are variable, it can be smaller than 10 mm, called microadenoma, it can be larger than 10 mm, called macroadenoma, or it can even be larger than 40 mm, called giant adenoma [2, 3]. The resection of the tumor is complex due to its narrow location, which requires experienced surgeons. The most common approach to treat PAs is the endoscopic transsphenoidal approach (ETA) surgery, a novel minimal invasive surgical technique performed by neurosurgeons and otolaryngologists [4]. It is the most used approach to treat PAs, since it does not require a craniotomy or external incisions, because the pituitary gland is accessed through the nasal passages, thus reducing the potential risks for iatrogenic damage. The surgeon inserts instruments, such as the endoscope, through the nose and accesses the sphenoid sinus with an incision in the posterior wall of the nasal septum. From the sphenoid sinus, the sella turcica is dissected to reach the tumor. The surgeon must ensure that the tumor is completely removed to prevent it from growing back from any remnants. Once the surgery is complete, the patient will have no visible scars. ETA has a considerable learning curve [5, 6] and it requires lots of experience to be performed safely, and such experience can be reached only after numerous surgeries in the operating room and with specific training [7]. The difficulty of this surgery is increased by the fact that, depending on the hardness of the tumor, the operating surgeon must choose the best strategy for the resection of the tumor. There are different degrees of hardness of the pituitary tumor which are grouped into five categories by Rutkowski *et al*, from 'cystic/hemorrhagic' to 'calcified' [8]. The different consistencies are related to the chemical compositions of the tumor [9]. Usually, softer PAs, the most common [10, 11], can be easily aspired while the harder ones require prior fragmentation [1, 12]. Knowing the hardness of the tumor before the surgery would allow surgeons to plan the most effective removal technique for the specific case, thereby reducing the risks to the patient however nowadays is still difficult to predict before approaching the tumor [13]. magnetic resonance imaging (MRI) is not sufficient to preoperatively predict the hardness of PAs. Nowadays, thanks to the advancement of research, radiomics analysis combined with artificial intelligence is becoming a great tool in predicting tumor hardness [13, 14]. What is still lacking is a mechanical characterization of the PA to evaluate, in a repeatable way, the hardness of the tumor. Several technologies have been proposed to estimate tissue stiffness or hardness, ranging from mechanical indentation tools [15] and capacitive or piezoresistive arrays [16] to fiber Bragg grating (FBG)-based sensors [17, 18] and advanced imaging modalities such as ultrasound shear wave elastography and optical elastography techniques [19], including optical time-harmonic elastography (OMTHE) [20]. These approaches have enabled valuable insights into tissue mechanical properties across various scales and clinical applications. However, despite recent progress, most existing systems face critical limitations when considered for intraoperative use. Mechanical Indentation Devices are not suitable for intraoperative or minimally invasive use due to size or manual operation. FBG or optical-based sensors are interesting solutions however they have complex optical routing and sensitivity to alignment or temperature. Finally, elastography techniques are not handheld nor contact-based in the sense of direct force application.

In this context, the solution proposed in this study—based on the integration of a tunnel magnetoresistance (TMR) sensor with a 3D-printed deformable tip—addresses these challenges effectively. By relying on magnetic field variation rather than direct mechanical or electrical contact, the device maintains a compact, enclosed architecture that is entirely sterilizable, while providing reliable, real-time estimation of tissue hardness through direct contact interaction. This makes it a promising candidate for intraoperative applications where size, sensitivity, and sterility are crucial. Specifically, in this work an attempt to characterize mechanically the hardness of PA is proposed using samples with similar mechanical properties as reported in the literature and described by surgeon experience. Measures were performed with a novel 3D printed sensor-based probe that can evaluate the hardness of soft biological tissues, such as PAs which was designed and initially validated in previous works [21, 22]. The advantage of this tool is its ease of manufacture, as it is designed for filament 3D printing techniques. It has also been tested with small deformations, in particular displacements of 1 mm, making it suitable for measuring small tissues such as a pituitary tumor. The concept at the basis of the probe consists of a highly flexible tip which deforms during indentation of the biological tissue. The flexibility of the tip is achieved using micro beams that are sensitive to the applied load. Moreover, the deformation of the tip is estimated using a tunneling magneto-resistive (TMR) sensor which measures the position of a magnet mounted on the tip. Since the harder the tissue the larger the deformation of the tip, it is possible to correlate deformation with hardness. Given the sub-millimetric dimensions of the tip beams, the research preliminary characterizes the 3D printing process

to determine the feasibility window of the micro-features and to determine how to control their dimensions, in particular the width. Then, tip designs different in beam width and number were fabricated and tested using samples with a hardness in the range from 51 to 83 on the Shore 000 scale (ASTM D2240). This range reflects the soft consistency typically observed in PA [10, 11]. The samples were tested using a cooked white egg which is adopted in the training of neurosurgeons to mimic the adenoma tissue [7, 23–28], and as confirmed in a training experience with expert neurosurgeons and otolaryngologists. Data are promising and show the best trade-off between sensitivity and stability, as the combination of the number of beams for the tip and their width shows a linear trend and a high repeatability of the tests. In the future, the aim is also to characterize not only the hardness of the PA but also in general of other soft biological tissues. The proposed sensor-based instrument aims to measure the hardness of the tumor *in-vivo*, during the minimally invasive transsphenoidal approach. The design of the instruments is determined by the geometric constraints of fitting into the nasal cavity and accessing the pituitary tumor in the sellar region. The current dimensions are determined by both the size of the circuit board and the 3D printing process. However, the overall dimensions are not the critical aspect on which the research is focused. This research is aiming at validating the measurements in terms of repeatability and accuracy to determine the hardness of soft tissue by studying the optimal geometry of the tip and its fabrication by changing the 3D printing parameters. The presented instrument can be listed in the electric-based sensor group determined, by Bandari *et al.* In their review [29], however, the innovative aspect is the use of a TMR sensor to evaluate the mechanical properties of soft tissues, i.e. hardness. This choice allows to have an enclosed environment in which the electronic is located, permitting all the sterilization processes. In addition, the proposed instrument is capable of measuring forces lower than 0.5 N, which are slightly lower, but comparable, to values found in the literature [30, 31], which, as pointed out by Bandari *et al* [29], can be a functional requirement to adopt for the development of a novel instrument for minimal-invasive surgery, as it is the transsphenoidal surgery.

2 The probe design

The probe consists of three parts: a rigid hollow structure named rigid case, a TMR sensor with a magnet and a highly deformable tip (figure 1). Moreover, dedicated assembly equipment was fabricated to support the mounting procedure. The tip consists of a top plate which is sustained by slender and highly flexible beams. The slender geometry of the beams makes their deformation sensitive to the hardness of soft materials when indented (figure 1(a)). In particular, the higher the hardness the higher the deformation. Furthermore, the magnet is mounted on the top plate while the TMR sensor is mounted in the rigid case (figure 1(b)). Therefore, when the tip indents a tissue and its beams flex, the position of the magnet to the sensor changes and the deformation of the tip can be measured. The instrument works similarly to a system of two elastic springs in series. When a compression stroke (or a compression Force) is applied to the system, springs are compressed, but their deformation is inversely proportional to their relative rigidity. In particular, the stiffer spring deforms less and the less rigid one deforms most. Moreover, if the stiffness of one spring and the total compression are known, it is possible to estimate the stiffness of the other spring by measuring its compression. Similarly, it is possible to correlate the hardness of the tested tissue with the deformation of the tip. In particular, this is possible if the deformation of the tip as the tissue hardness changes has been previously characterized.

21. *The rigid case*

The rigid case consists of a hollow cylinder in which the printed circuit board (PCB) with TMR sensor is inserted (figure 1). It has an external diameter of 5.6 mm and a thickness of 0.25 mm in the thinnest section. It presents 0.3 mm depth external grooves used to position the beams of the tip (figure 1). The rigid case was 3D printed in Pearl-White PLA on the Ultimaker 3 extended machine (both by Ultimaker, Netherlands). Moreover, the AA025 nozzle (0.25 mm diameter) was used due to the low dimensions of the part. Cura slicing software was used with default printing parameters for material and nozzle.

22 *The TMR sensor*

The TMR sensor used is an Ultra High Sensitivity TMR linear sensor model TMR2905S (MultiDimension Technology Co., Ltd, China). The main advantage of TMR sensors is that they can be sealed inside a magneto-transparent material thus eliminating the risk of contact with biological liquids. The TMR sensor, with dimensions of 3 × 3 mm, is soldered onto a PCB with dimensions of 4.2 × 22 mm (figure 1) and measures the variation of the magnetic field caused by the displacement of the magnet attached to the tip. Accordingly, the TMR sensor was characterized.

23. *The highly deformable tip*

The tip consists of a flat circular plate from which several beams extend radially, with the number of beams (N) varying. The plate has a diameter of 3.2 mm, the beams are 15 mm in length and their width (w) may vary (figure 2(a)). The overall thickness of the tip (t) is uniform and equal to 0.45 mm as the best value in terms of sensitivity found in previous research [22]. The tip is 3D printed with flexible material on a flat surface. In particular, to enhance the flexibility of the beams, they are printed as a single line of material extruded by the nozzle

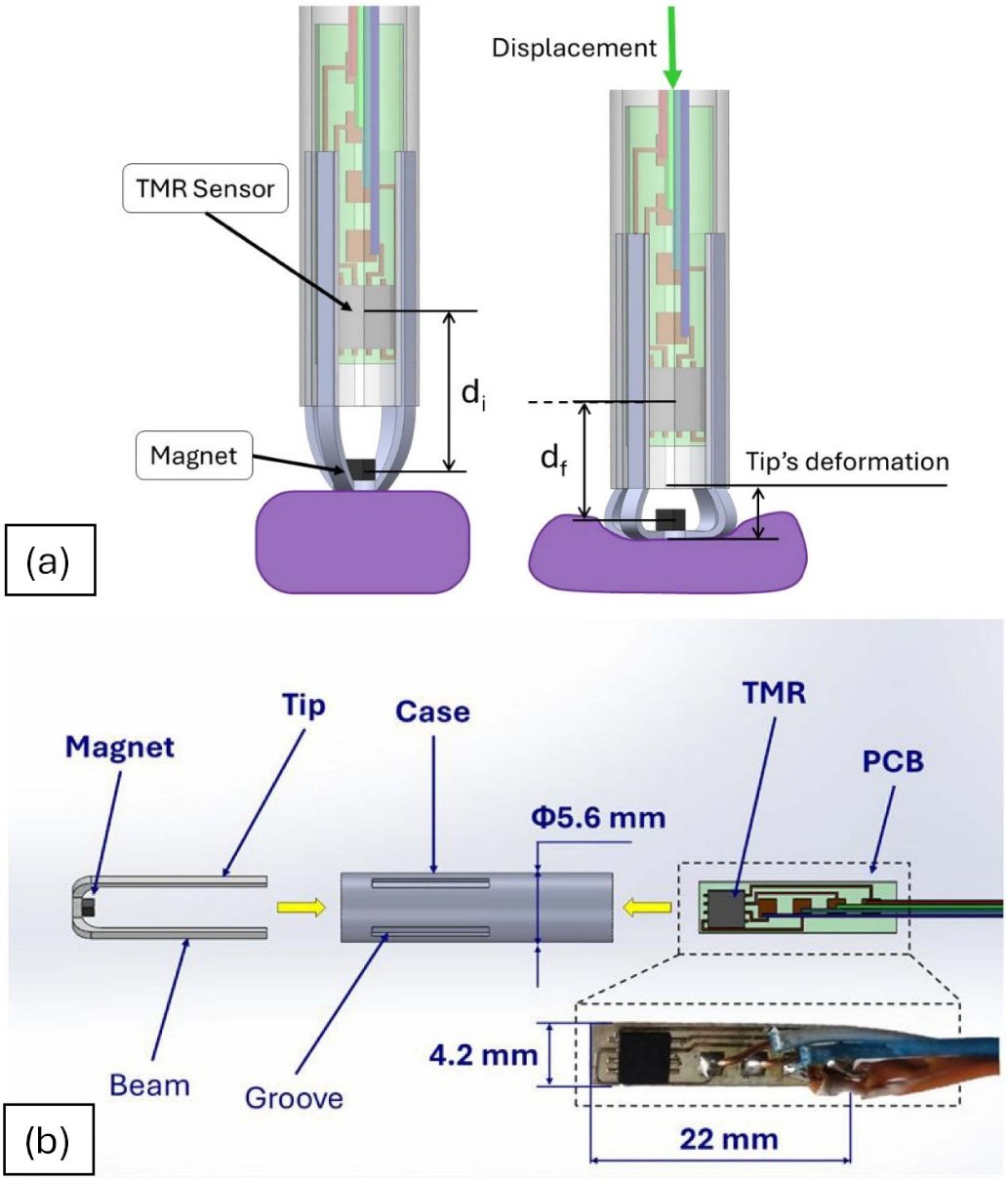

Figure 1. (a) The tip is composed of a deformable top plate supported by slender beams that flex under load. When the tip indents a tissue, the resulting deformation—modulated by tissue hardness—shifts the position of a magnet mounted on the plate relative to a fixed TMR sensor in the rigid case. (b) An exploded view of the various components with some dimensions. The external diameter of the rigid case is 5.6 mm as it must be thin enough to pass through the nasal cavities, on the side there are different grooves to guarantee a repeatable mounting phase of the probe. On the top of the probe, there is a square hole designed to hold the board with the TMR sensor soldered. The TMR sensor is soldered to a PCB with a width of 4.2 mm and a length of 22 mm.

(figure 2(b)). This print was obtained by studying the interaction of three different printing parameters: print speed (v_0), line width (w_0), and layer height (h_0). These parameters are discussed in greater detail in the following sections. The magnet is 1x1x1 mm in dimension and it is glued at the center of the circular plate. Finally, the tip is folded and attached to the rigid part of the probe (figure 1), as reported by previous works [21, 22]. The tip represents the core element of the probe. For this reason, part of the research focuses on the optimization of its manufacturing and geometry as described in the following sections.

2.4. *The assembly equipment*

Previous works highlighted how the small sizes of the device make it difficult to correctly position the magnet on the tip [21, 22]. Therefore, equipment to align and position the magnet on the tip was designed and 3D printed in PLA on

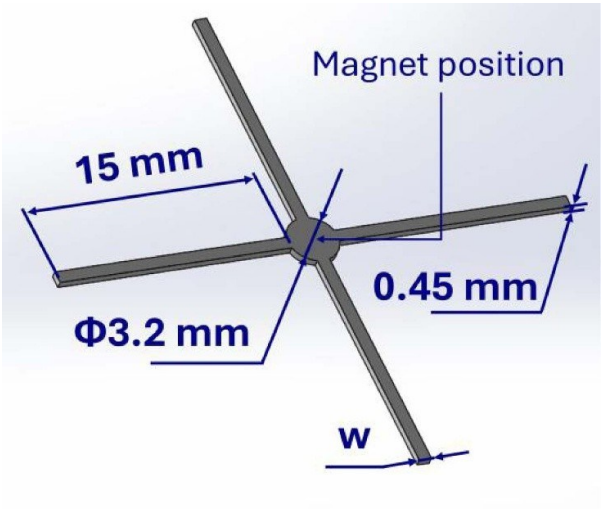

(a)

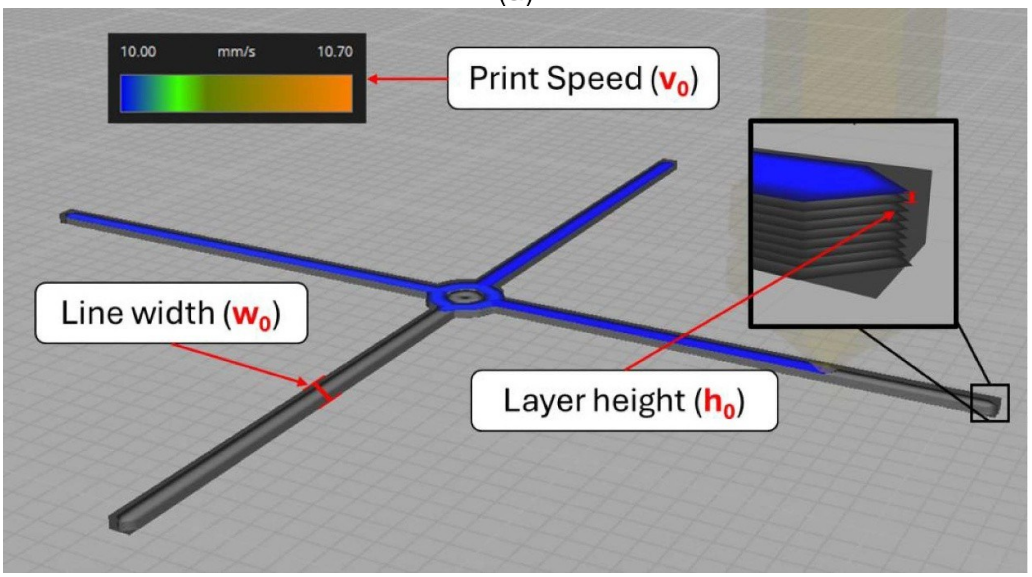

(b)

Figure 2. The diameter of the circular base is 3.2 mm, the length of a single beam is 15 mm, while the overall thickness is 0.45 mm. The magnet is positioned in the middle of the circular base (a). To enhance the sensitivity of the tip, its beams are printed as a single line of material extruded by the nozzle.

Ultimaker 3 extended with a 0.4 mm nozzle. The device uses a magnetic field to orientate the small cubical magnet with the center tip. In particular, the equipment (figure 3) consists of a base which holds 3 cylindrical magnets with a diameter of 5.6 mm and a height of 9 mm (figures 3(a) and (b)), and a tip holder which aligns the tip with the axis of the cylindrical magnets. The tip holder can be customized according to the dimensions and the number of beams (N) of the tip. The assembly procedure involves placing the tip on the holder and applying a drop of acrylic glue onto the circular base and, finally, dropping the small cubic magnet. By gravity and magnetic fields, the cubic magnet self-aligns at the center of the circular plate.

3. Experimental setup

The experimental setup used to design, fabricate, and characterize the proposed probe comprises three main components: the 3D printing system for the mechanical parts, a custom electronic setup for data acquisition, and a set of reference instruments for material and dimensional verification. These include a Shore 000 hardness tester (Axiotek SRL, Italy), with a measurement uncertainty of 1 Shore 000 unit, and an optical microscope (Quick Scope, Mitutoyo Corporation, Japan) for dimensional measurements. The 3D printer and the electronic setups are described below.

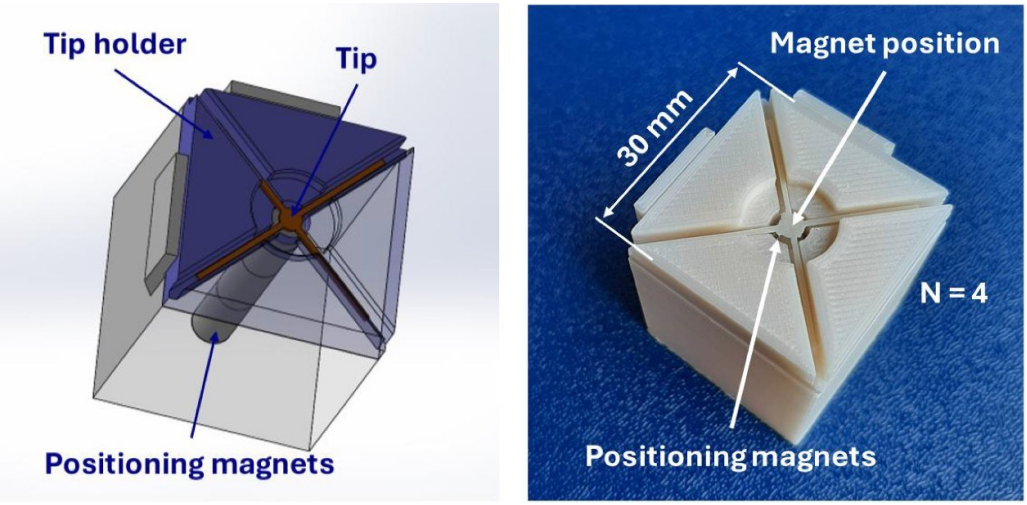

(a) (b)

Figure 3. Positioning equipment. The equipment is designed to guarantee a repeatable positioning of the magnet in the middle of the tip, on the left the CAD design (a) on the right the instrument printed (b).

Table 1. Mechanical properties of Pearl-White PLA and TPU 95 A. XY, YZ and Z refer to the orientation of the specimen tested, X-Y is the printing plate, while Z t is the printing direction. Data are taken from their respective technical datasheets [32, 33]. As mentioned in the datasheets, tests are performed following the ISO 178 regulations. NB = No Break (>10%).

		Value (orientation)		
Mechanical property	Material	(XY—Flat)	(YZ—Side)	(Z—Up)
Flexural modulus (MPa)	PLA	3019 ± 87	2894 ± 53	2740 ± 47
Flexural strain at break (%)		4.8 ± 0.2	NB	1.9 ± 0.2
Hardness (Shore D scale)		84		
Flexural modulus (MPa)	TPU 95 A	62.6 ± 1.7	55.1 ± 2.4	62.6 ± 2.0
Flexural strain at break (%)		NB	NB	NB
Hardness (Shore D scale)		48		

3.1. 3D printing setup

Two different materials were chosen for the fabrication of the probe parts: the rigid case and the highly deformable tip, each fabricated using fused filament fabrication (FFF). To provide the required stiffness to the rigid case, it was chosen PLA, one of the most common 3D printing materials and therefore one of the least expensive: it was used the Pearl—White PLA filament, one of the PLA produced by Ultimaker. The filament used has a diameter of 2.85 mm and it was printed using the AA025 print-core to reproduce both the small details of the rigid case and its overall size. To print the highly deformable tip, a different material was found to be the best solution in terms of lower rigidity of the printed parts. The material chosen was the thermoplastic polyurethane (TPU) 95 A by Ultimaker, another common and low-cost 3D printing material, which is suitable for printing flexible components, i.e. the tip. The TPU 95 A filament used has a diameter of 2.85 mm and it was printed using the AA04 print-core, a print-core with a diameter of 0.4 mm. Concerning the choice of materials TPU has a flexural strength, and a flexural strain lower compared to PLA, which means that it is more suitable to produce highly deformable parts as the tip. A more detailed comparison between these two materials is shown in table 1, where are reported data from the technical datasheet of the materials: PLA [32] and TPU [33]. Flexural modulus and flexural strain at break are reported considering the orientation of the specimen during printing, in particular: XY refers to the plane of the printing plate, while Z is the direction of the printing (perpendicular to the printing plate).

3.2 Electronic setup

The complete characterization setup includes the sensorized probe mounted on a precision load cell that is fixed to a motorized micrometric translation stage. This configuration enables controlled indentation of the probe tip into the test sample. The TMR sensor, embedded in the probe, has a supply voltage of 1 V and the load cell of 10 V with a sensitivity of 4.353 (N mV^{-1}) as resulted in a previous characterization [34]. A multimeter (model 34401A, Agilent Technologies, Inc., USA)

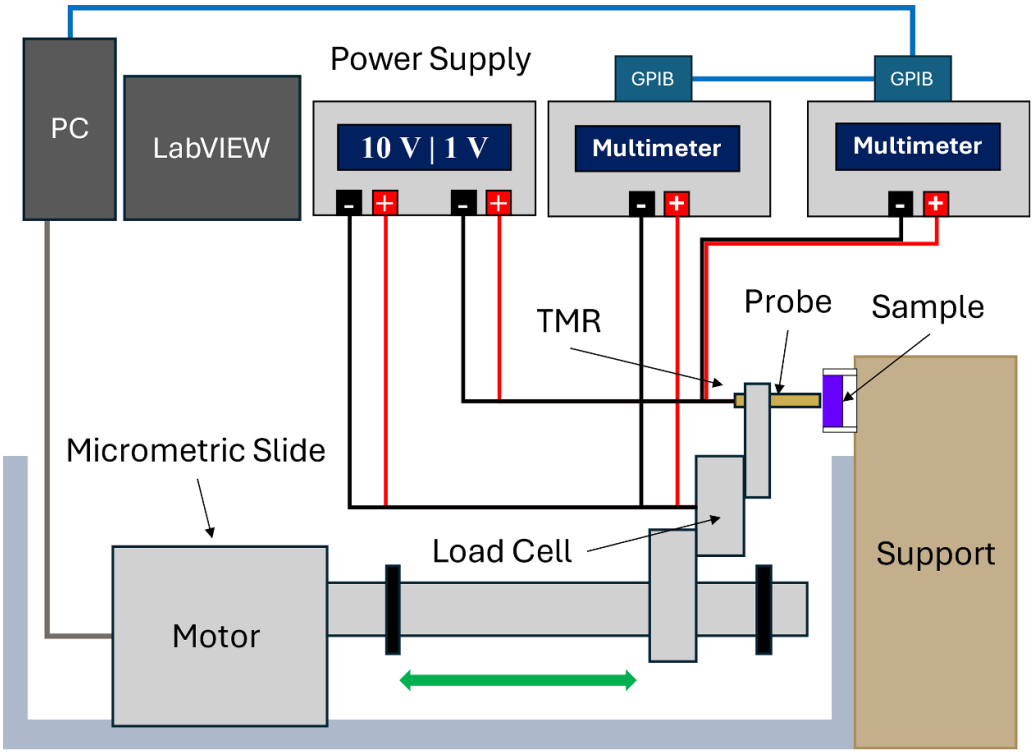

Figure 4. The electronic setup. The probe is moved against a sample by a micrometric slide whose position and speed are computer controlled. The TMR sensor has a supply voltage of 1 V and the load cell of 10 V with a sensitivity of 4.353 (N mV^{-1}). A multimeter collects the signal from the TMR sensor, which is related to the deformation of the tip, while a second multimeter collects the signal from the load cell, which is related to the force applied to the tip. Data are acquired with a LabVIEW program at a sampling rate of 2.00 Hz.

Table 2. The electronic setup used for testing.

Component	Model	Specifications	Use	Notes
Power supply	PL330DP	Independent channels	To power the load cell at 10 V and the TMR sensor at 1 V.	—
Multimeter 1	HP 34401A	Resolution: $6^1/_2$ digits	To read the load cell data.	—
Multimeter 2	HP 34401A	Resolution: $6^1/_2$ digits	To read the pressure sensor data.	—
Micrometric Slide	—	Resolution: 0.010 mm	To move the probe.	Computer controlled
Load Cell	—	Sensitivity: 4.4 N mV^{-1}	To measure the contact force.	—
TMR Sensor	TMR2905S	Dimensions: 3.0 × 3.0 mm Uncertainty: 4.7×10^{-4} V	To measure the variation of the magnetic field generated by a magnet glued to the tip.	Soldered on a PCB of 4.2 × 22 mm
GPIB-USB-HS interface	—	—	To allow simultaneous collection of both sensors.	—
LabVIEW	—	Sample rate: 2.00 Hz	To obtain data during tests.	—

collects the signal from the TMR sensor, which is related to the deformation of the tip when indented on a sample, while a second multimeter (model 8840A, Fluke Corporation, USA) collects the signal from the Load Cell (figure 4), which is related to the force applied to the tip (table 2). Data acquisition is performed using LabVIEW (National Instruments, USA) at a sampling rate of 2.00 Hz. The setup allows for synchronized acquisition of force and displacement signals, which are used to evaluate the performance of the probe in estimating tissue hardness.

3.3. *TMR characterization*

Before starting the experimental campaign, the TMR sensors were characterized to establish the correlation between the sensor output (in volts) and the distance between the sensor

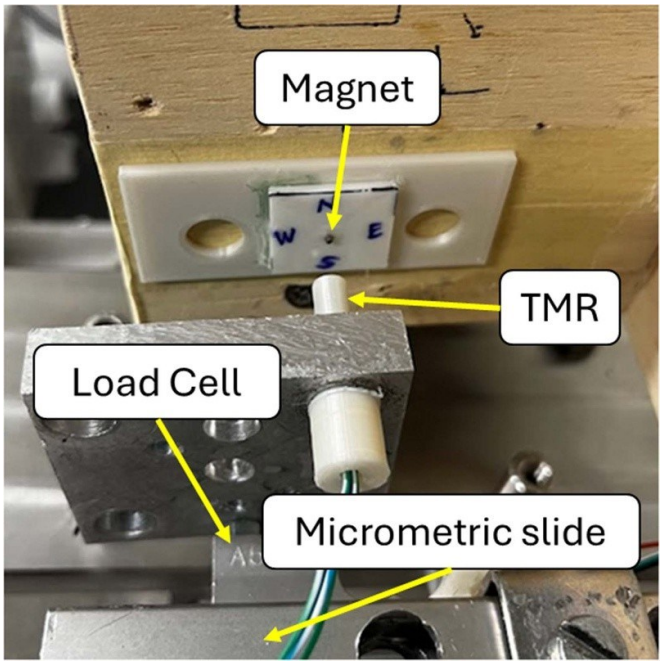

Figure 5. TMR characterization setup. equipment for the characterization test on the TMR sensor.

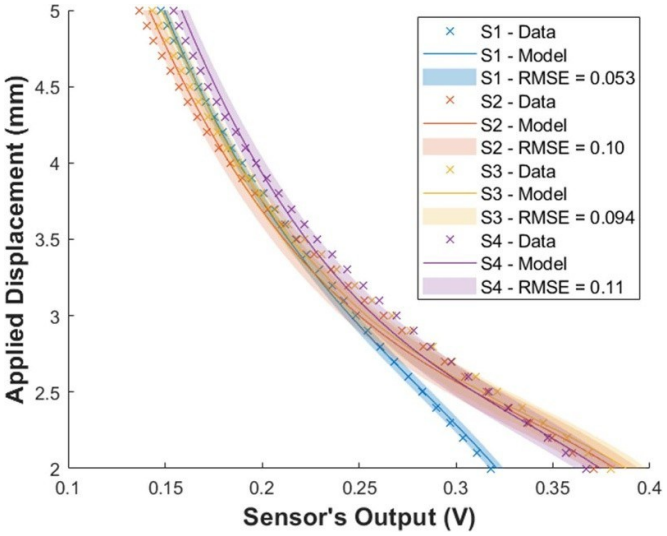

Figure 6. TMR characterization curve. Results of the characterization tests performed on the TMR sensors. As already mentioned, from our preliminary tests, the TMR sensor used has a measurement uncertainty of 4.7 × 10 − 4 V, while the resolution of the micrometric slide is 0.01 mm. The four TMR sensors data (S1, S2, S3 and S4) were interpolated using a 3rd degree linear model. S1 has an RMSE of 0.053, S2 has an RMSE of 0.10, S3 has an RMSE of 0.094 while S4 has an RMSE of 0.11, the R^2 for each model is >0.99. Regression models were performed on a sample size of 71 for each sensor.

and the magnet (in millimeters). For this purpose, the PCB with the TMR sensor was mounted in the rigid case without the deformable tip. A cubic magnet (1 × 1 × 1 mm) with the negative polarity facing the sensor was placed in front of the case, as illustrated in figure 5. The characterization procedure involved placing the rigid case in contact with the magnet, which was defined as the zero-distance reference. The magnet was then moved away to a distance of 10 mm, followed by a stepwise approach with 0.1 mm increments until contact was re-established. At each step, the output voltage of the TMR sensor and the corresponding distance were recorded. A total of four TMR sensors (S1–S4) from the same batch were characterized and later used in the experimental tests (figure 6). The measurement uncertainty was evaluated as the standard deviation of the sensor output at 10 mm over repeated displacement cycles and was found to be 4.7 × 10^{-4} V, assumed consistent across all sensors. The data collected for each sensor were fitted using a third-degree polynomial regression model. The root mean square errors (RMSE) were 0.053 for S1, 0.10 for S2, 0.094 for S3, and 0.11 for S4, with coefficients of determination (R^2) exceeding 0.99 in all cases. Each model was based on a dataset of 71 measurements.

4. Experimental tests and results

The beams of the tip represent the key features of the probe since the response of the sensor mostly depends on their flexibility. Accordingly, two experimental campaigns were conducted to properly design the probe. The first campaign aims at characterizing the printing process to identify how the process parameters influence the cross-section of the beams, and, in particular, the width (w) of the printed lines. The width was measured using an optical microscope by Mitutoyo (figure 7(a)), with its integrated software (figure 7(b)). The second campaign aims at the optimization of the tip geometry by investigating the correlation between width (w) and the number of beams (N) and the behavior of the probe in terms of sensitivity, linearity and uniformity amongst the fabricated probes.

4.1. Process characterization

Three process parameters were considered to characterize the process: the layer height (h_0), the nominal line width (w_0) and the print speed (v_0). Their values were chosen based on default print settings (w_0 = 0.40 mm, v_0 = 25 mm s^{-1}) and preliminary tests. In particular, they showed that w_0 should vary in the range of 0.20 ÷ 0.80 mm (approximation of the values suggested by the slicing software). Moreover, printing becomes unstable (i.e. discontinuous extrusion) for v_0 > 50 mm s^{-1} in every combination of the other process parameters.

Accordingly, different combinations of parameters were progressively tested to print single lines of 30 mm in length with a nominal width of w_0 (table 3 and figure 8). For handling reasons, multiple layers of lines were printed to a height of 0.90 mm and then measured in width. Results were evaluated in terms of process feasibility, line width and material flow through the nozzle. The process feasibility was evaluated in terms of material extruded from the nozzle and, in the case of discontinuous extrusion, the process was considered failed. Moreover, the widths of the sample were measured in three

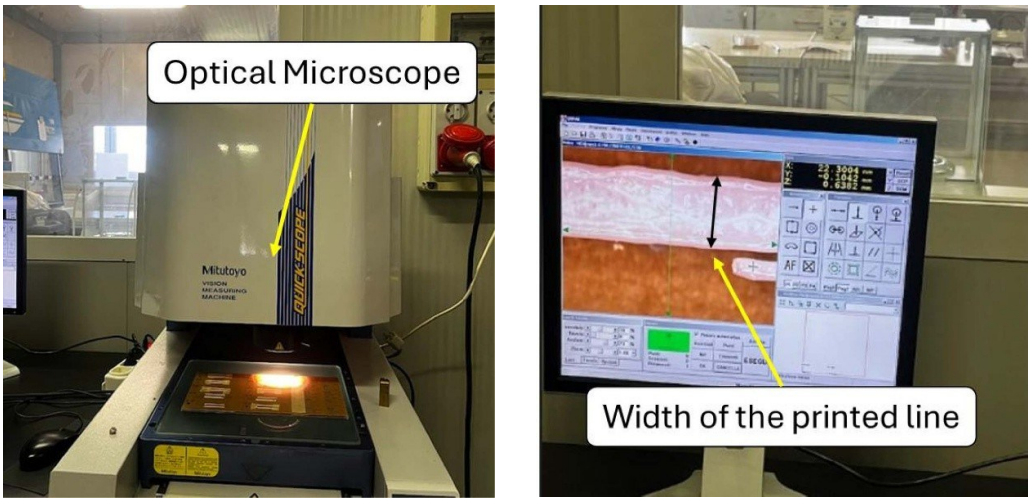

Figure 7. The width of the printed lines was measured with the quick scope optical microscope by Mitutoyo (Mitutoyo corporation, Japan) (a), the measurements were performed using its embedded software (b).

Table 3. Characterization tests. Summary of the tested parameters.

Printing parameter	Values	Units
Layer height, h_0	0.05–0.10–0.15	mm
Line width, w_0	0.20–0.26–0.30–0.40–0.50–0.60–0.70–0.80	mm
Print speed, v_0	2.0–5.0–15–25–37.5–50	mm s^{-1}

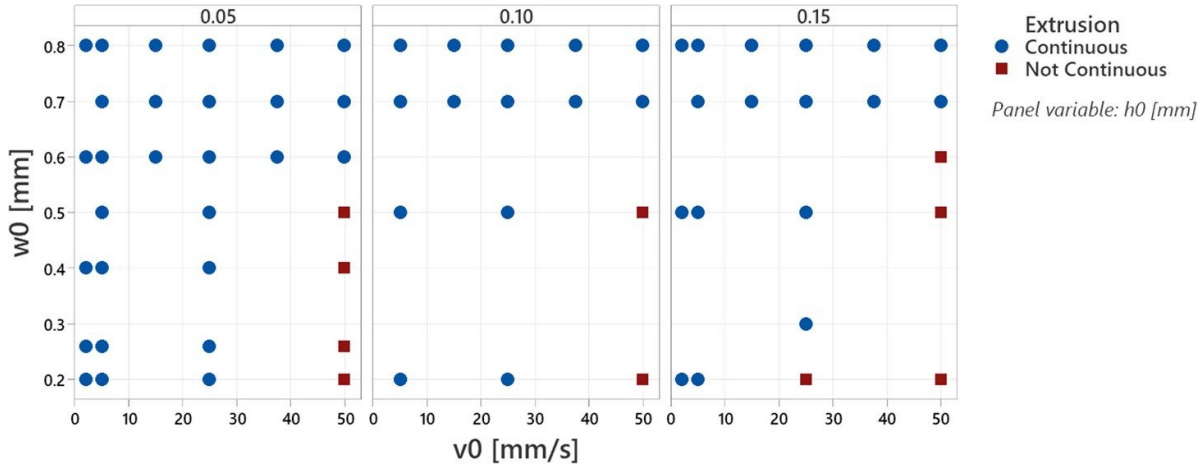

Figure 8. Characterization tests. Summary of the tests conducted to characterize the process on the variation of the layer height (h_0), line width (w_0) and print speed (v_0). Circles represent the continuous extrusion, and squares represent the discontinuous extrusion. The polygonal and rectangular boxes represent respectively the domains of the general and local regression models for line width control.

different positions and mean value (w) and standard deviation ($w_{st.dev}$) were calculated.

Results showed the feasibility limits of the process and its repeatability. Moreover, they were used to characterize the effects of the process parameters: h_0, w_0, v_0 on the width (w) of the printed line.

Figure 8 shows that, in general, a higher print speed (v_0) leads to a discontinuous extrusion of material for mid or low values of nominal line width (w_0). Given the unfeasibility of the process in those conditions, failed tests were excluded in the following analysis.

The ratio w/w_0 in figure 9 shows that the width of the printed line (w) is different from the nominal one (w_0) as other process parameters change. In particular, the higher the print speed (v_0), the lower the ratio w/w_0. This shows that w_0 does not control, completely nor partially, the actual line width (w) of the printed line. Moreover, it can explain the effect of the print speed (v_0) on material extrusion in figure 8. In fact, as

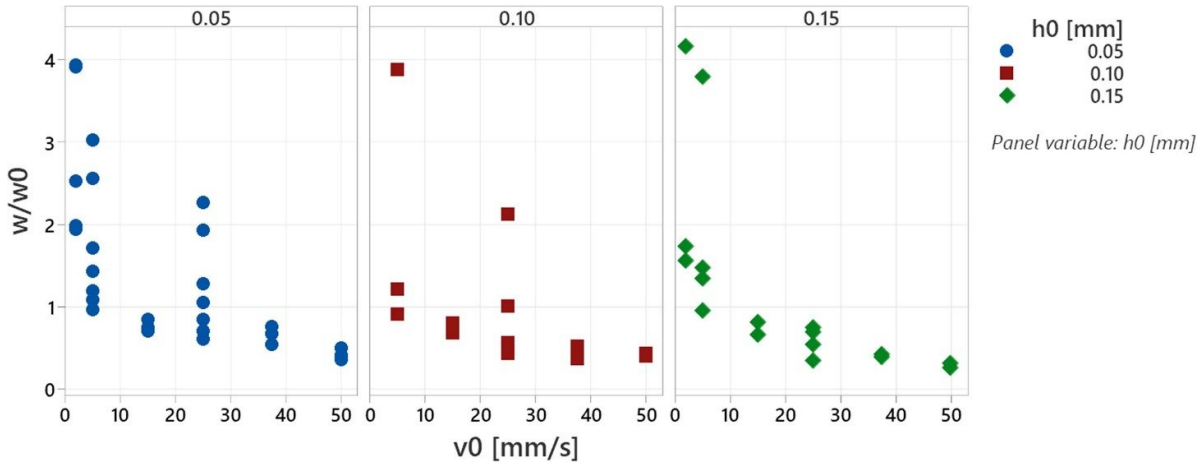

Figure 9. Ratio w/w_0. Comparison between the printed (w) and nominal (w_0) width values as layer height (h_0) and print speed (v_0) changes.

the print speed increases, the 3D printer does not successfully compensate for the line width (w) which, at the highest speed, becomes too low so compromising the adhesion of the material on the underlying layer. Hence, a discontinuous extrusion occurs.

For these reasons, the results were analyzed to determine how to effectively control the width of the printed lines which are directly correlated to the actual 3D printed geometry of the tip beams. Then, a regression model of the process able to predict the line width (w) as a function of the process parameters was developed.

To identify the process window of the regression (i.e. the dataset to be used), some preliminary considerations were drawn on the behavior of the width of the printed lines. Figure 10 reports the average width value (w) and its standard deviation ($w_{st.dev}$) in each line printed. In particular, it shows that a lower sprint speed (v_0) leads to less uniform lines (figure 10(b)), especially for v_0 = 2 mm s^{-1}. Therefore, these tests were excluded from the regression analysis. Moreover, when the process is limited to h_0 = 0.05 mm and v_0 = 5.0–50 mm s^{-1}, the width w_0 has a lower or negligible influence on the average value (w) (figure 10(a)) and the standard deviation ($w_{st.dev}$) is the lowest (figure 10(b)). Hence, the process is more robust, and printed lines are more uniform in this range of parameters.

Based on previous considerations, two regression models were developed using two different subsets of data. The first dataset is wider (figure 8, dot-dashed boxes) and contains all feasible tests where the process is sufficiently uniform, that is all tests conducted at v_0 = 5.0–50 mm s^{-1}, failed test excluded. The second one is local (figure 8, dashed box) and contains the tests where the process is more uniform and robust, that is h_0 = 0.05 mm, w_0 = 0.60–0.80 mm and v_0 = 5.0–50 mm s^{-1}. For each domain, a regression model was identified, named general and local models. An initial polynomial model including grade 3 terms and grade 2 interactions was considered. Then, the corrected Akaike information criterion was used to exclude the non-significant terms (alpha-value = 0.05) and to develop the final regression models.

The general regression model (w_G) is reported in (1) and in figure 11 and has an R^2 = 0.89. It is a grade 3 polynomial function in v_0 and includes all other tested parameters as interactions between h_0 and both v_0 and w_0. Moreover, print speed (v_0) mostly influences the final width (w) while other parameters have a minor influence (figures 11(a) and (b)). This is in accordance with what was previously discussed about the influence of the process parameters (figures 8 and 9)

$$w_G = 0.86 - 0.033 \cdot v_0 + 0.00098 \cdot v_0^2 - 0.054 \cdot h_0 v_0 + 0.94 \cdot h_0 w_0 - 0.000010 \cdot v_0^3. \quad (1)$$

The local regression model (w_L) is reported in (2) and in figure 12, has an R^2 = 0.97. Different from the general regression model, the local model is a grade 3 polynomial function in v_0 only (figure 12(a)). Therefore, print speed (v_0) is the only parameter that influences the final width (w) while other parameters have no effects (figure 12(b)). This is compliant with the robustness of the process that was previously observed when h_0 = 0.05 mm (figures 8 and figure 12(a))

$$w_L = 0.94 - 0.046 \cdot v_0 + 0.0015 \cdot v_0^2 - 0.000018 \cdot v_0^3. \quad (2)$$

The regression models were validated by 3D printing a set of tips using five different print speeds (v_0 = 5.0, 10, 25, 37.5 and 50 mm s^{-1}) with constant nominal line width (w_0 = 0.8 mm) and layer height (h_0 = 0.05 mm). According to the design of the tip described previously, the thickness (t) of the tips is equal to 0.45 mm and three different numbers of beams (N = 3, 4 and 5) were considered.

The width of the printed tips was measured three times for each beam and the mean value (w) and its standard deviation ($w_{st.dev}$) were estimated. Results were compared with the values predicted by the global (w_G) and local (w_L) regression models. In particular, $w \pm 3 \cdot w_{st.dev}$ was adopted to consider the 99.7% variability. Tests at v_0 = 37.5 mm s^{-1} and 50 mm s^{-1} were excluded because it was not possible to successfully remove them from the build plate. In fact, the smaller width (w) and thickness of the part (t) resulted in a part cross-section too weak to handle. Results (table 4) show that

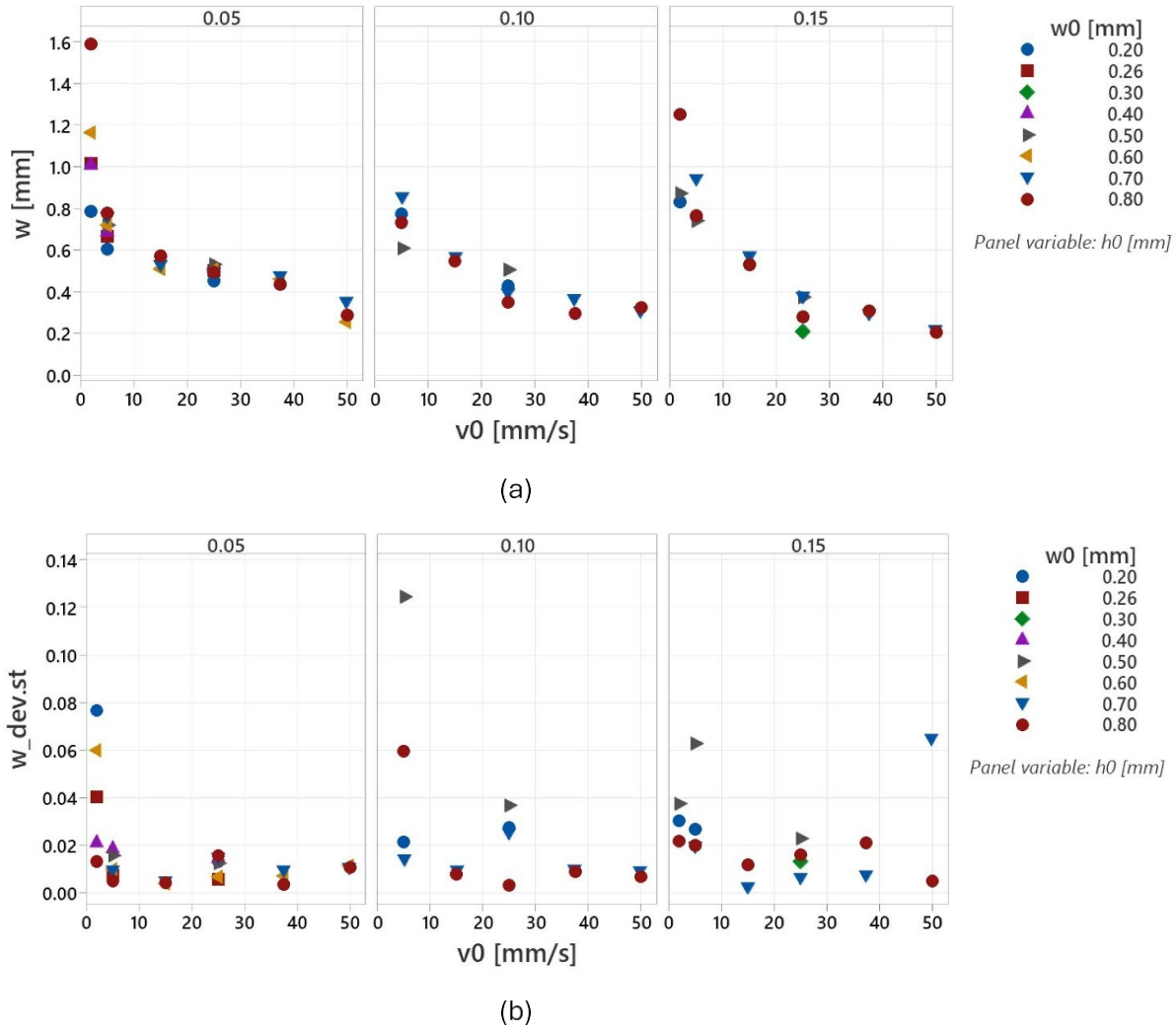

Figure 10. Line average width (w) and variability ($w_{st.dev}$). (a) Average width (w) and (b) standard deviation ($w_{st.dev}$), of the width of the 3D printed lines as other the process parameters nominal line width (w_0), layer height (h_0) and print speed (v_0) change. Standard deviation is estimated on the repeated measures of each single line printed.

the prediction of both models falls within 99.7% of the measure variability, even though they show an overestimation tendency. This could be related to the lower thickness of the part (0.45 mm) than the one used to collect the data for the model (0.90 mm). In fact, a greater height increases the number of misaligned layers leading to a greater width of the part and, thus, to an overestimation of the line width (w).

Accordingly, the previous discussion and considerations can be summarized as follows:

- The sprint speed (v_0) is the parameter that most influences the width of the printed lines (w). A speed range of 5.0 ÷ 50 mm s^{-1} can be adopted for a layer height h_0 = 0.05 mm and nominal line width w_0 of 0.60 ÷ 0.80 mm. As h_0 increases or w_0 decreases, the maximum print speed (v_0) should be lowered.
- The nominal line width (w_0) parameter marginally controls the width of the printed line (w). Moreover, if a layer height h_0 = 0.05 mm is adopted, the influence of w_0 is not statistically significant.
- At higher print speed (v_0), the lower width (w) of the lines could limit the handling of the part (in particular, its removal from the build plate). Hence the number of layers (i.e. thickness of the part) should be increased to enhance its resistance.
- A lower layer height (h_0) leads to more uniform printed lines. Moreover, when h_0 = 0.05 mm and v_0 = 5 ÷ 50 mm s^{-1}, the process is more robust (i.e. independent from w_0), and the line width (w_0) can be controlled through the print speed (v_0) only.
- The local regression model developed is more accurate and robust and it should be preferred to model the influence of print speed (v_0), on the line width (w_0), of the 3D printed lines.
- As the number of layers increases, the misalignment of the printed lines may lead to greater overall part width

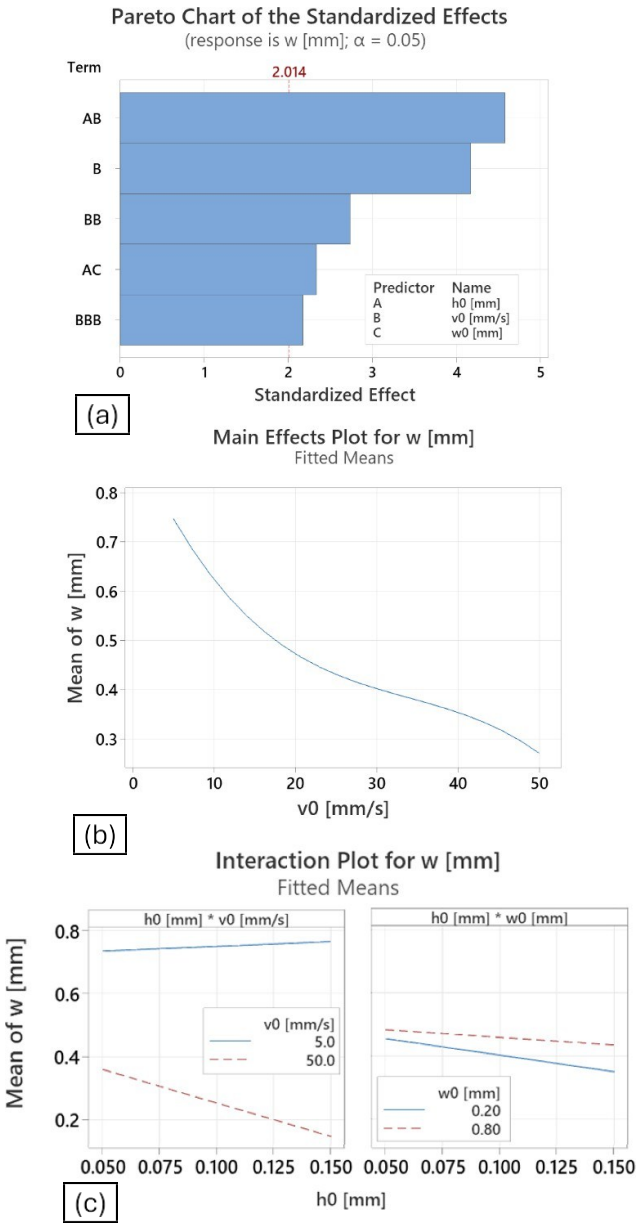

Figure 11. Global regression model. Characterization of the influence of the process parameters on the line width (w) in the process window: $h_0 = 0.05 \div 0.15$ mm, $w_0 = 0.2 \div 0.8$ mm, $v_0 = 5.0 \div 50$ mm s^{-1}, failed test excluded. (a) Pareto chart and (b) main effects plot for w and (c) interaction plots of the regression model.

(w). Therefore, when the part thickness is different to the one used to develop the regression model, a final measurement should be performed to verify the actual part width. Otherwise, the regression model could be extended including the influence of the part height.

4.2 Tip optimization

The optimization of the tip design was performed using the tips printed to validate the regression models. Accordingly, 3 values of print speed (v_0) with 3 numbers of beam (N) and 2 replicates for each design were tested (table 5 and figure 13) for a total of 18 tips. The tips were assembled (figure 14) as described in figure 1 and then tested.

4.3 Indentation tests

The experimental setup described in section 3 was used to test the tips. In particular, the indentation test procedure consists in:

- *First contact.* The tip is moved against the sample using a 0.10 mm step motion. First contact is detected through the axial force measured by the load cell. The initial contact between the probe and the sample is identified through the force signal measured by the load cell, which is currently required to calibrate the deformation model used for hardness estimation.
- *Indentation*. The probe moves 1.00 mm towards the sample at 1.00 mm s^{-1} and holds for 1 min, then returns. The first

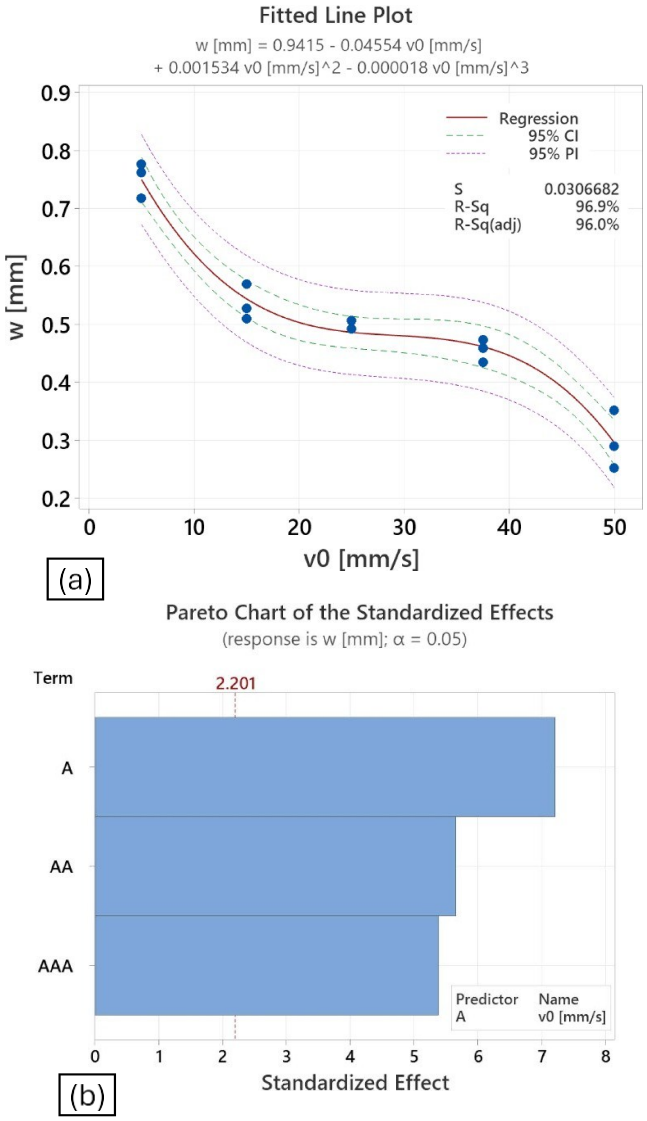

Figure 12. Local regression model. Characterization of the influence of the process parameters on the line width (w) in the process window: h_0 = 0.05 mm, w_0 = 0.60 ÷ 0.80 mm, v_0 = 5.0 ÷ 50 mm s^{-1}. Plots of the regression model (a). Pareto chart (b).

Table 4. Models validation. Width of the printed tips (w) compared with the prevision of the global (w_G) and local (w_L) regression models.

v_0	Tips (mm)	Prediction (mm)		Difference (mm)	
(mm s^{-1})	$w \pm 3 \cdot w_{st.dev}$	w_G	w_L	$w_G - w$	$w_L - w$
5	0.63 ± 0.18	0.74	0.75	0.12	0.12
10	0.50 ± 0.12	0.63	0.62	0.13	0.12
25	0.41 ± 0.050	0.47	0.48	0.050	0.060

Table 5. Tip design tests. Parameters adopted to evaluate and optimize the design.

Tip design	Values	Units
Print speed (v_0)	5.0–10–25	mm s^{-1}
Beams (N)	3–4–5	—
Thickness	0.45	mm
Layer height (h_0)	0.050	mm
Line width (w_0)	0.80	mm

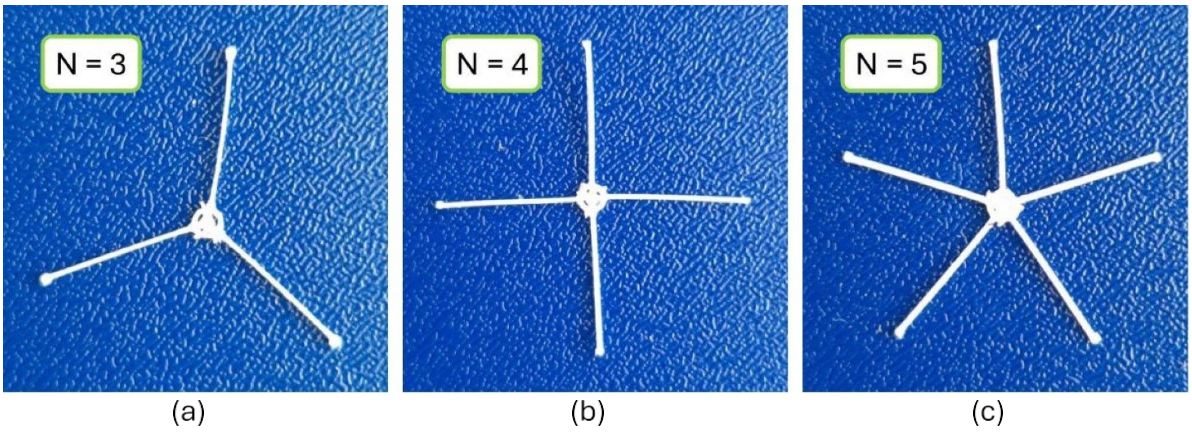

Figure 13. Examples of printed tips. Printed tips with different number of beams (N). $N = 3$, $N = 4$ and $N = 5$ (a), (b) and (c) respectively.

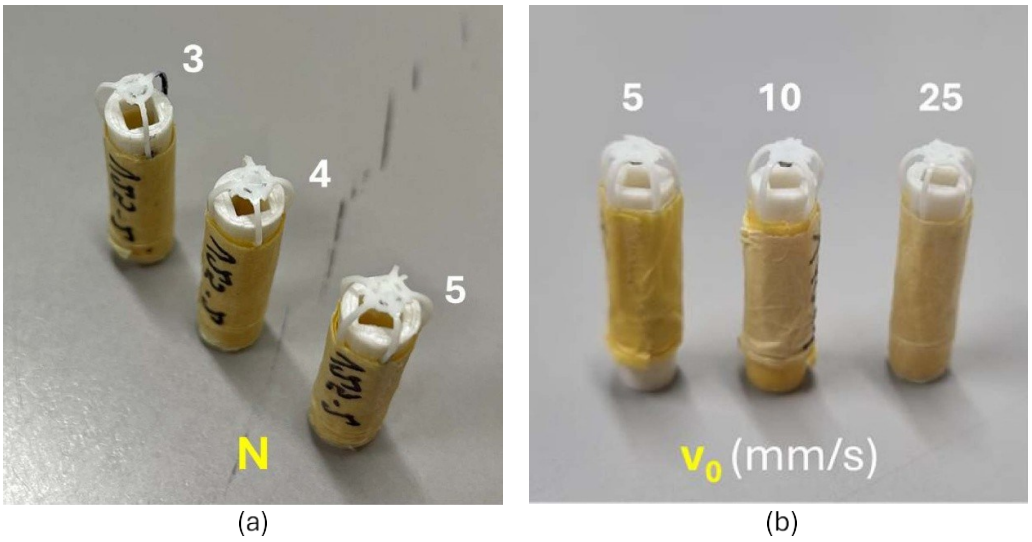

Figure 14. Probes assembled. Probes with a different number of beams $N = 3$,4 and 5 (a). Probes with $N = 5$ printed with different print speeds $v_0 = 5$, 10 and 25 mm s^{-1} (b).

indentation is used to settle the tip and therefore discharged. Then, indentation is repeated 3 times on the tested sample.

- *Data acquisition*. During indentation, signals from load cells and TMR are collected and converted respectively in contact Force and distance of the tip (i.e. magnet) from the sensor.

Silicone samples having different hardness from 51 ± 1–83 ± 1 Shore 000 hardness (figure 16(a)) together with a Marshmallow with a measured Shore 000 hardness of 51 ± 1, and a boiled egg white sample with a hardness of 52 ± 1 Shore 000 hardness (figure 16(b)) were used to characterize the probes during indentation tests. No human samples or biological tissues of human origin were used in this study. The egg white was obtained by cooking in 113 g of raw egg white in microwave at 800 W for 70 s, then the sample was obtained by manually cutting a square in the center of the boiled egg white. The hardness of the samples (figure 15) was measured using the Shore 000 durometer described in section 3 entitled 'Experimental setup'.

The typical profiles of contact Force and tip distance signals detected during indentation tests are reported in figure 16. The force, figure 16(a), rapidly reaches the peak during indentation, then it decreases while the probe holds contact. When the probe returns to the initial position, the force becomes negative and then it settles to the null value. The initial peak of the force may be influenced by dynamic effects and the following reduction derives from an assessment of the system (as discussed below). Moreover, the negative force values indicate that the probe is temporarily pulled, probably due to a temporary adhesion between the surfaces of the probe and the sample. The distance between the tip and the TMR sensor, reported in figure 16(b), is similar to the force profile. In particular, it shows a large reduction during indentation followed by a lower further reduction during the hold phase which confirms an assessment of the system.

The results of the tests were compared using the force (F) at the end of the hold phase (matt symbols in figure 16(a)) and the compression of the tip ($h_{\%}$). In particular, $h_{\%}$ expresses the compression of the tip and is calculated using equation (3)

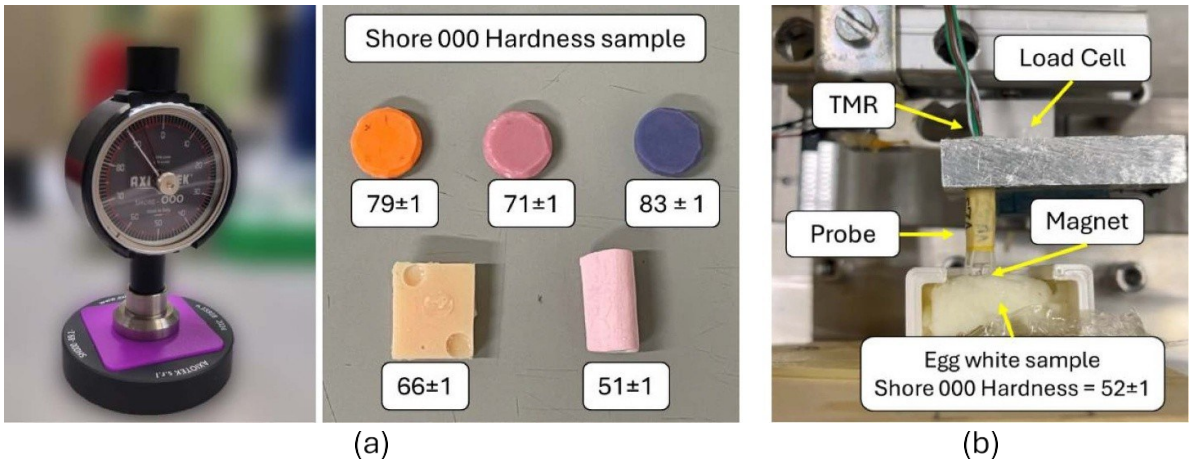

Figure 15. The Shore 000 durometer, the silicone samples with the Marshmallow (a). The probe pressed against the egg-white sample, during indentation tests (b).

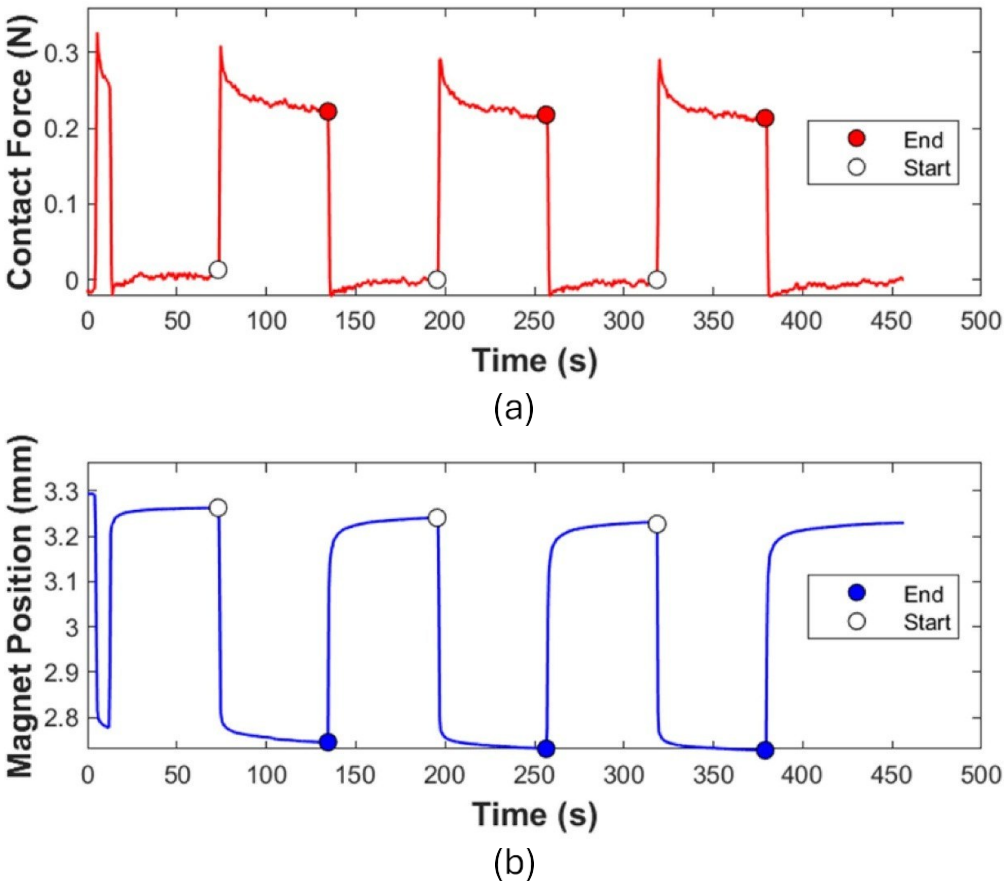

Figure 16. Results of the indentation test. (a) 'Contact force' on the tip detected by the load cell and (b) the 'magnet position', or the tip displacement detected by the TMR sensor.

where d_0 is the displacement imposed at the probe and d is the difference between the initial and the final distances of the tip from the TMR sensor (respectively empty and matt symbols in figure 16(b)), as reported in previous works [15, 16]

$$h_{\%} = \frac{d}{d_0} \cdot 100. \quad (3)$$

The results of the experiments are reported in figures 17 and 18 respectively in terms of the average values of F and $h_{\%}$ upon the 3 indentations. Moreover, data were linearly interpolated as a function of the hardness (dashed lines) and RMSE of the regressions was estimated (shaded area). Finally, the regressions were inversely used to estimate the egg hardness through the experimental results (F and $h_{\%}$) and the prediction

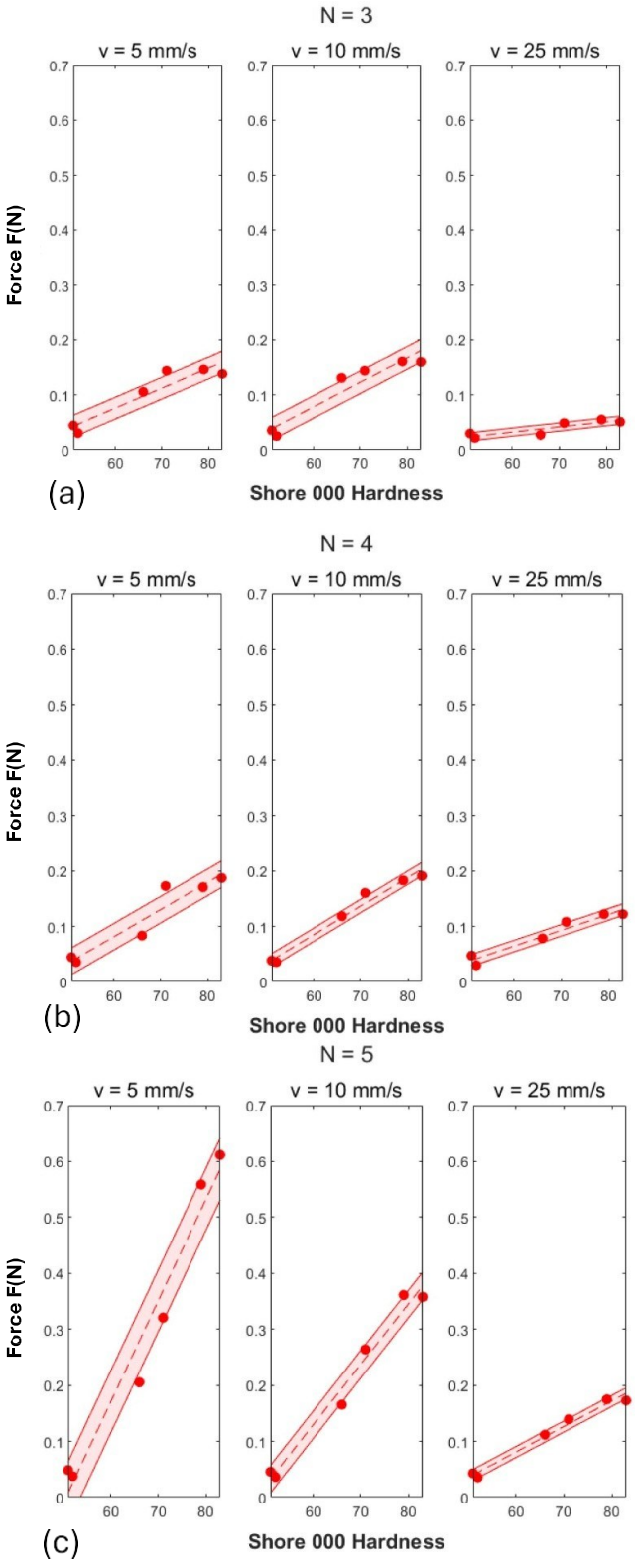

Figure 17. Indentation test—Force (F) results. The contact force between the probe and the samples as the material hardness, number of beams (N) and printing speed (v_0) change. The dashed lines represent the linear regression model, colored areas are the RMSE. (a) Number of beams (N) = 3, (b) N = 4 and (c) N = 5.

was compared with the actual hardness of the egg white sample (52 ± 1 Shore 000 hardness). The summary of the regressions is reported in table 6.

The sensitivity of force (F) to the hardness of the samples (figure 17) depends on the number of beams (N) and the print speed (v_0). This becomes more evident when the force slopes for $N = 5$ are compared. In fact, the force required to compress the tip depends on its stiffness which, in turn depends on the number of beams (N) and their width (w) which is influenced by v_0 as reported in figures 18 and 19. In particular, less beams (N) and a lower width (w, which corresponds to higher v_0) reduce the stiffness of the tip with a loss of the force sensitivity. Overall, the response is generally almost linear and RMSE values are small. Moreover, if the $h_{\%}$ value is considered (figure 18), the tests with $v_0 = 10$ mm s^{-1} provide less scattered results. The higher scattering of the results when lower or higher speed are considered can be explained as follows. Low values of v_0 lead to a lower uniformity of the beam width (w in figure 10(a)) which may affect the uniformity of the mechanical properties of the probes. Moreover, higher values of v_0 lead to thinner beams that are more difficult to manipulate during the assembly, reducing the precision in the alignment of the tips.

The sensitivity of tip deformation ($h_{\%}$) to the sample hardness (figure 18) less depends on the tip design and makes this index generally more robust than the force (F). This is confirmed by figure 19 which compares the actual hardness of the white egg sample with the ones predicted by the regression models. In particular, the values predicted using $h_{\%}$ (figure 19(b)) are more precise and less variable than the ones obtained using F (figure 19(a)). Figure 19 also shows that the accuracy of the prediction of the egg hardness varies with the tip design. In particular, the most performant cases that were previously identified ($N = 5$ and $N = 5$ using $v_0 = 10$ mm s^{-1}) provide a good prediction, especially when $h_{\%}$ is considered. In other cases, the prediction is highly variable, especially in the case of the tip with $N = 3$ and $v_0 = 25$ mm s^{-1}. This case is characterized by the lowest sensitivity of the tip with respect to the force (figure 17 and table 6), a medium-to-high RMSE value for the tip deformation (figure 18 and table 6) and the highest scattering in the prediction of the boiled egg hardness (figure 19). Together, these factors may have contributed to the low accuracy of the prediction.

On the contrary, linearity and RMSE depend on the tip design (table 6). In particular, the most performing tips are the ones printed with a speed $v_0 = 10$ mm s^{-1} which have the strongest linear trend (i.e. highest Adj.R^2) and, in cases of $N = 4$ and $N = 5$, the lowest RMSE. Furthermore, the error of these two probes in predicting the hardness of boiled white egg is −1.90% and 0.00% respectively. Finally, the indentation force during white egg tests is lower than 0.050 N, which is slightly lower, but comparable with data presented in literature [24, 25]. This validates the capability of the probes to characterize the hardness of a biological tissue-like material.

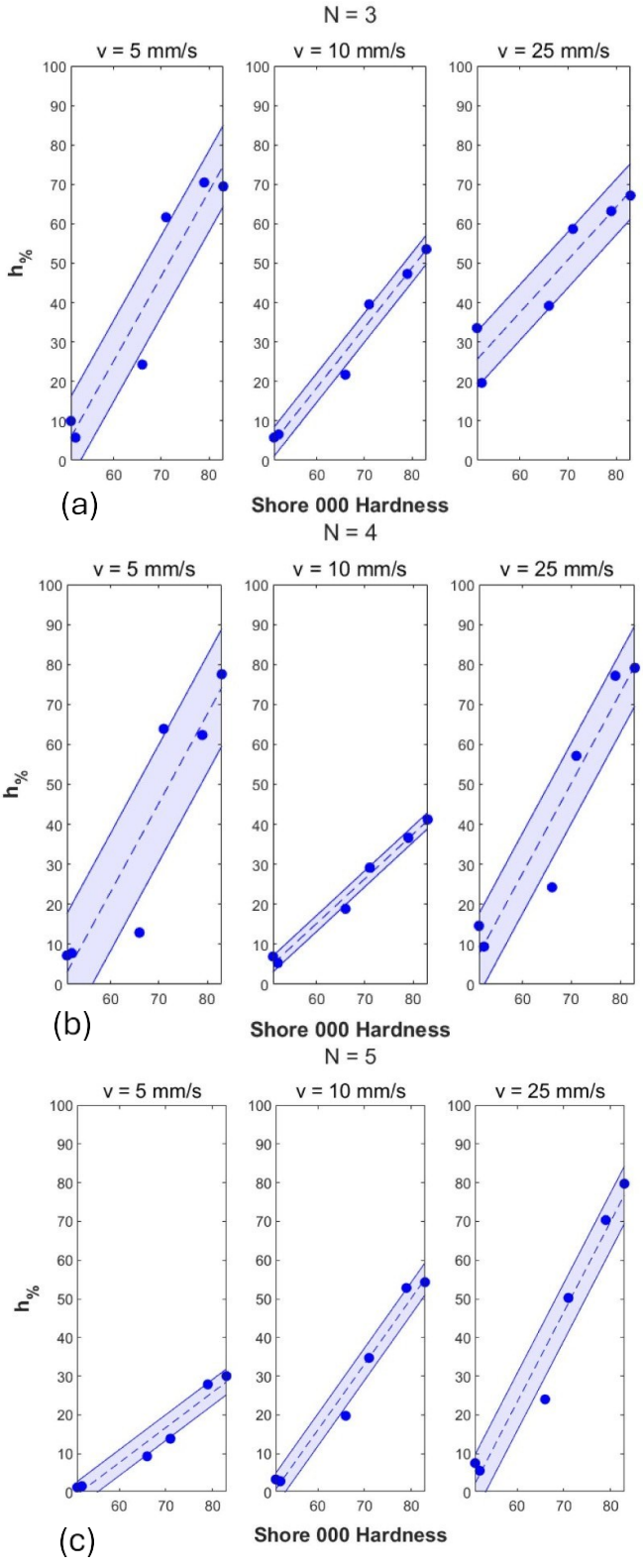

Figure 18. Indentation test—Compression (h%) results. Compression of the tip as the material hardness, number of beams (N) and printing speed (v_0) change. The dashed lines represent the linear regression model, colored areas are the RMSE. (a) Number of beams (N) = 3, (b) N = 4 and (c) N = 5.

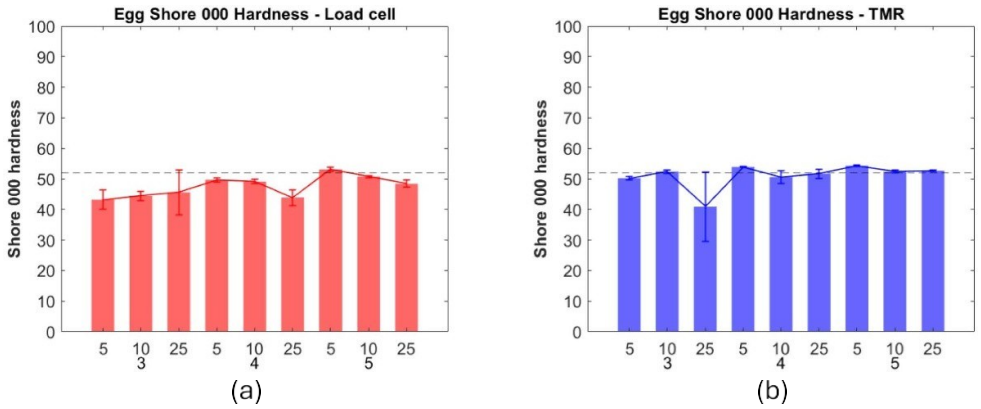

Figure 19. Sample hardness prediction. Comparison of the experimental hardness of the boiled white egg (52 Shore 000 Hardness) with the values predicted using the trends of contact force (F) and tip compression ($h_{\%}$) (a) and (b) respectively.

Table 6. Regression models: in this table are reported the most important results obtained with the regression model, obtained from load cell data. Abbreviations: m = slope of the regression model; adj. R^2 = adjusted R^2; RMSE = root mean square error; Pred. Sh000 = Predicted Shore 000 hardness of the Egg sample from the Linear regression model; $\Delta_{\%}$ = percentage variation between the measure obtained with the Shore 000 hardness durometer and the value predicted from linear models.

Tests		Contact Force—F, load cell					Deformations—h%, TMR				
		Model			Pred. Sh000		Model			Pred. Sh000	
N	v_0	m	adj. R^2	RMSE	Egg	Δ%	m	adj. R^2	RMSE	Egg	Δ%
3	5	0.0031	0.80	0.019	43	−17%	2.1	0.82	12	50	−3.8%
3	10	0.0039	0.86	0.020	44	−15%	1.5	0.95	4.3	52	0.00%
3	25	0.00084	0.58	0.0083	46	−12%	1.1	0.84	6.03	41	−21%
4	5	0.0047	0.82	0.027	50	−3.8%	2.3	0.73	17	54	3.8%
4	10	0.0049	0.96	0.012	49	−5.8%	1.1	0.97	2.2	51	−1.9%
4	25	0.0025	0.93	0.0083	44	−15%	2.2	0.85	12	52	0.00%
5	5	0.018	0.93	0.063	53	1.9%	0.94	0.91	3.7	54	3.8%
5	10	0.011	0.96	0.028	51	−1%–9%	1.7	0.95	4.8	52	0.00%
5	25	0.0043	0.97	0.0092	48	−7.7%	2.4	0.92	8.6	53	1.9%

Comparing all tested cases, the tip deformation $h_{\%} = 0$ corresponds to a Shore 000 hardness of approximately 50. This value represents a lower limit for the application of the probe, a limit that probably can be overcome by increasing the flexibility of the tips.

Additionally, the repeatability of the behavior of the samples was evaluated. In particular, the standard deviations of the force (F) and the tip deformation ($h_{\%}$) are reported in figure 20. For each test, a total of 36 measures were considered, corresponding 2 replicas of the probe, 6 samples indented, and 3 indentations each. Results reported in figure 20 show that the probes designed with $N = 4$ beams and fabricated with a print speed of $v_0 = 10$ mm s^{-1} show good repeatability both in F and $h_{\%}$. Moreover, if $h_{\%}$ only is considered, tips with $N = 5$ and $v_0 = 5$ mm s^{-1} and 10 mm s^{-1} also can be considered for their good repeatability. Overall, this result confirms the results in figures 17 and 18.

The results and discussion can be summarized as follows:

- The indentation force suggests that relief and sticking effects may occur between the probe and the sample. This may be related to the couple of materials and needs to be verified when actual tissues are indented.
- The index $h_{\%}$ is more robust than force in the prediction of the sample hardness. Therefore, the probe that has been presented is preferable to load cells for this application.
- Tips printed with a speed $v_0 = 10$ mm s^{-1} show a more linear response of $h_{\%}$ to the tissue hardness.
- Tips printed with a speed $v_0 = 10$ mm s^{-1} and $N = 4$ provide more repeatable results for both F and $h_{\%}$.
- The best performance in terms of linearity and low RMSE of $h_{\%}$ were obtained with the tip having $N = 4$ beams and printed with speed $v_0 = 10$ mm s^{-1}. Similar results were achieved with $N = 5$ and $v_0 = 10$ mm s^{-1}, but with a lower repeatability of the compression force (F). Overall, the developed probes are capable of predicting the hardness of materials in the range of 51 ± 1–83 ± 1 Shore 000 hardness. Outside this range, the tested probes are not usable.

5. Discussion and conclusions

This work presents the design and optimization of a miniaturized, sensorized probe capable of discerning the hardness of soft anatomical tissues, with a particular focus on PAs. The probe is intended to assist surgeons in intraoperatively

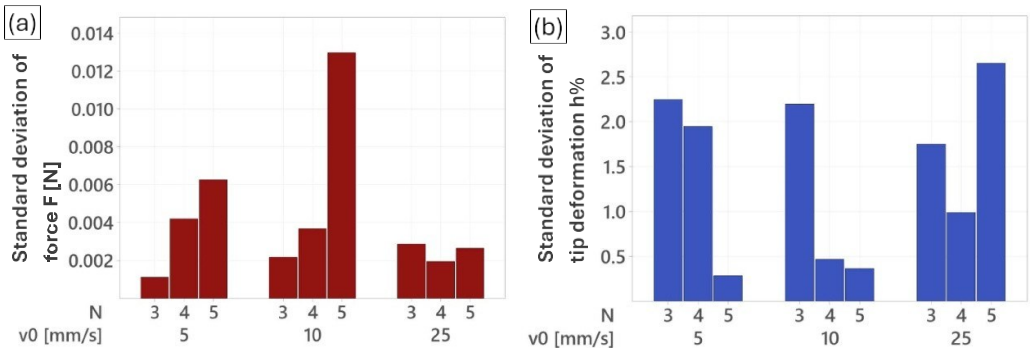

Figure 20. Repeatability of the behavior of the samples. (a) Standard deviations of the force (F) and (b) of the tip deformation (h%).

assessing tumor consistency prior to resection. During surgery, it could be inserted transnasally and gently pressed against the exposed tumor mass, providing objective and real-time feedback on tissue hardness to support surgical decision-making. The probe consists of a highly deformable tip, a TMR (tunnel magnetoresistance) sensor with a magnet, and a rigid outer case. Its working principle relies on how the tip deformation varies when pressing against tissues of different hardness: the stiffer the tissue, the greater the resulting tip deflection. The tip features a flat end supported by slender beams that flex during indentation, with the magnet mounted on the deflecting end. The TMR sensor measures the magnet's displacement, allowing the deformation—and thus the tissue hardness—to be estimated. The development process faced several challenges, including miniaturization to enable transnasal insertion (target width: 4–5 mm), sub-millimetric features for tip flexibility, and reliable performance for tissue stiffness estimation. The deformable tips were fabricated using FFF 3D printing, and a dedicated characterization of the printing process was performed to control feature dimensions. Subsequent optimization involved designing, fabricating, and experimentally evaluating multiple probe variants, ultimately leading to the selection of an optimal design validated using adenoma tissue-mimicking materials. Regarding the materials selected for the probe components, including the deformable tip and rigid casing, they are compatible with common sterilization techniques such as ethylene oxide and low-temperature plasma sterilization, although further validation is required to ensure compliance with clinical sterilization standards and protocols.

When compared with existing tissue stiffness sensing technologies (see table 7), the proposed approach offers a balanced trade-off between compactness, sensitivity, and clinical compatibility. Mechanical indentation tools offer high-resolution data but are bulky and unsuitable for intraoperative use. Capacitive and piezoresistive sensors, though flexible, struggle with calibration and limited penetration depth. FBG sensors and optical systems provide good sensitivity and MRI compatibility but require complex setups and are prone to environmental disturbances. Elastography-based imaging techniques deliver excellent spatial resolution and non-invasiveness, yet they are not handheld, contact-based, or easily deployable in real time.

In contrast, the proposed probe fills a key gap in this technological landscape. It combines sensitivity to indentation for forces less than 0.050 N, repeatability for force measurement less than 0.004 N, estimation of the hardness of materials with errors below 2%, and with a compact, customizable, and sterilizable design. Though it requires physical contact and is limited to superficial measurements, these characteristics align well with the anatomical and procedural constraints of endonasal neurosurgery. The probe's localized stiffness measurement capability and ease of integration with surgical tools make it a promising candidate for intraoperative applications.

The results achieved are very promising, with the best-performing designs showing sensitivity and accuracy suitable for clinical applications. The probe will be further developed by testing real biological tissue to evaluate its performance and validate it in the surgical field. Some aspects require further improvements. The first is related to the range of tissue hardness that can be tested; more sensitive tips should be developed to extend the measurable range beyond the current limits. Additionally, the current overall width of the probe is slightly larger than the desired specifications, mainly due to the PCB board and case size. Future work will explore alternative miniaturization techniques for these components to comply with surgical requirements. Looking ahead, several directions for future research and development can be envisioned. One important step will be the integration of the probe with surgical robotic tools, which could enhance precision and ease of use during operations. Moreover, *in vivo* validation using animal models or cadaveric tissues will be essential to confirm the probe's performance in realistic clinical conditions. Efforts will also focus on improving the mechanical deformation models and developing algorithms that rely solely on the TMR sensor data for contact detection and stiffness estimation, potentially removing the need for external force sensors. Beyond hardness measurement, there is interest in integrating additional types of sensors into the probe to monitor other relevant tissue parameters, broadening its diagnostic capabilities. Finally, refining the assembly and manufacturing process will be crucial to reduce variability and ensure consistent performance across probes. These advancements will contribute to making the probe a valuable clinical tool, providing surgeons with objective, real-time information to support better surgical decision-making.

Table 7. Comparison between the methods reported in the literature.

Category	Performances	Advantages	Limitations
Mechanical indentation	Forces > 98 N; P–h curve with 3 distinct loading stages; Signals correlate with fracture events [15]	High mechanical resolution; it provides fracture insights	Invasive; unsuitable for *in vivo* use; bulky equipment
Capacitive/piezoresistive tactile sensors	Sensitivity up to GF = 476; response time 6–200 ms; strain range 0%–80% [16]	Flexible, wearable, suitable for soft robotics	Calibration challenges; non-uniform sensitivity; limited depth penetration
Fiber Bragg Grating (FBG) sensors	Real-time strain sensing; stiffness extracted from force–strain data [17]	Miniaturizable; good sensitivity; surgical tool integration	Temperature-sensitive; requires optical demodulation setup
	Overview of 47 MRI-compatible optical sensors; various physiological signals [18]	Electromagnetic immunity; compatible with MRI environments	Costly optical setup; complex calibration
Advanced imaging techniques	Construct validity $r = 0.99$; inter/intrarater ICC > 0.85 [19]	Portable; low-cost; easy to operate	Validated only on phantoms; lower precision than imaging-based methods
	Multiscale resolution (μm to mm); rapid stiffness mapping [20]	Non-invasive; high resolution; deep tissue mapping	Complex setup; high cost; not yet feasible for real-time clinical use
Proposed method	Sensitivity to indentation for forces <0.050 N; repeatability < 0.004 N for force; errors less than 2%	Compact; customizable; localized stiffness measurement; surgical integration potential	Limited depth penetration; requires physical contact

Data availability statement

All data that support the findings of this study are included within the article (and any supplementary files).

Declaration of generative AI and AI-assisted technologies in the writing process

During the preparation of this work the authors used 'DeepL Write' and 'Grammarly' to improve language and readability. After using these services, the authors reviewed and edited the content as needed and take full responsibility for the content of the publication.

References

[1] Smith K A, Leever J D and Chamoun R B 2015 Prediction of consistency of pituitary adenomas by magnetic resonance imaging *J. Neurol. Surg. B* **76** 340–3

[2] Russ S, Anastasopoulou C and Shafiq I 2024 Pituitary adenoma *StatPearls* (StatPearls Publishing) (available at: www.ncbi.nlm.nih.gov/books/NBK554451/) (Accessed 7 August 2024)

[3] Lu B, Zhang Y, Liu C, Ma X, Liu G, Bie Z, Yang Z and Liu P 2023 Intraoperative cerebrospinal fluid leakage and residual tumors in endoscopic transsphenoidal surgery for pituitary adenoma: risk analysis and nomogram development *Acta Neurochirurgica* **165** 4131–42

[4] Doglietto F, Prevedello D M, Jane J A, Han J and Laws E R 2005 A brief history of endoscopic transsphenoidal surgery—from Philipp Bozzini to the first world congress of endoscopic skull base surgery *Neurosurg. Focus* **19** 1–6

[5] Ahn Y, Lee S and Shin D-W 2024 Learning curve for endoscopic transsphenoidal surgery: a systematic review and meta-analysis *World Neurosurg.* **181** 116–24

[6] Berhouma M, Baidya N B, Ismaïl A A, Zhang J and Ammirati M 2013 Shortening the learning curve in endoscopic endonasal skull base surgery: a reproducible polymer tumor model for the trans-sphenoidal trans-tubercular approach to retro-infundibular tumors *Clin. Neurol. Neurosurg.* **115** 1635–41

[7] Santona G *et al* 2023 Training models and simulators for endoscopic transsphenoidal surgery: a systematic review *Neurosurg. Rev.* **46** 248

[8] Rutkowski M J *et al* 2020 Development and clinical validation of a grading system for pituitary adenoma consistency *J. Neurosurg.* **134** 1800–7

[9] Wei L, Lin S, Fan K, Xiao D, Hong J and Wang S 2015 Relationship between pituitary adenoma texture and collagen content revealed by comparative study of MRI and pathology analysis *Int. J. Clin. Exp. Med.* **8** 12898–905

[10] De Alcubierre D *et al* 2023 Pituitary adenoma consistency affects postoperative hormone function: a retrospective study *BMC Endocr. Disorders* **23** 92

[11] Yamamoto J, Kakeda S, Shimajiri S, Takahashi M, Watanabe K, Kai Y, Moriya J, Korogi Y and Nishizawa S 2014 Tumor consistency of pituitary macroadenomas: predictive analysis on the basis of imaging features with contrast-enhanced 3D FIESTA at 3T *Am. J. Neuroradiol.* **35** 297–303

[12] Acitores Cancela A, Rodríguez Berrocal V, Pian H, Martínez San Millán J S, Díez J J and Iglesias P 2021 Clinical relevance of tumor consistency in pituitary adenoma *Hormones* **20** 463–73

[13] Hassan R M A *et al* 2024 Predicting the consistency of pituitary macroadenomas: the utility of diffusion-weighted imaging and apparent diffusion coefficient measurements for surgical planning *Diagnostics* **14** 493
[14] Bioletto F, Prencipe N, Berton A M, Aversa L S, Cuboni D, Varaldo E, Gasco V, Ghigo E and Grottoli S 2024 Radiomic analysis in pituitary tumors: current knowledge and future perspectives *J. Clin. Med.* **13** 336
[15] Faisal N H, Reuben R L and Ahmed R 2011 An improved measurement of vickers indentation behaviour through enhanced instrumentation *Meas. Sci. Technol.* **22** 015703
[16] Bandari V, Akyildiz A C and Ahn C H 2022 Recent advances in flexible and stretchable tactile sensors for soft robotics *Sens. Actuators A* **332** 113077
[17] Padmanaban S, Kanakambaran S and Subbaraj P K 2024 Stiffness assessment in tissue grasping using surgical tool integrated with fiber Bragg grating sensor *Proc. IEEE Int. Conf. Electronics, Computing and Communication Technologies (CONECCT)* (https://doi.org/10.1109/CONECCT62155.2024.10677085)
[18] Dziuda Ł 2015 Fiber-optic sensors for monitoring patient physiological parameters: a review of applicable technologies and relevance to use during magnetic resonance imaging procedures *J. Biomed. Opt.* **20** 010901
[19] Brandl A, Acikalin E, Bartsch K, Wilke J and Schleip R 2024 Reliability and validity of an app-assisted tissue compliance meter in measuring tissue stiffness on a phantom model *PeerJ* **12** e17122
[20] Jordan J *et al* 2024 Optical time-harmonic elastography for multiscale stiffness mapping across the phylogenetic tree *Adv. Sci.* **11** 24010473
[21] Santona G, Fapanni T, Fiorentino A, Doglietto F and Serpelloni M, 2023 Preliminary study on a 3D printed sensorized probe to characterize pituitary adenoma hardness *2023 IEEE Int. Workshop on Metrology for Industry 4.0 & IoT (Metroind4.0&iot)* pp 249–53
[22] Santona G, Fiorentino A, Doglietto F and Serpelloni M 2024 A novel 3D printed sensorized surgical instrument to characterize pituitary adenoma: development and initial validation *2024 IEEE Int. Workshop on Metrology for Industry 4.0 & IoT (Metroind4.0 & IoT)* pp 7–11
[23] Okuda T, Kataoka K and Kato A 2010 Training in endoscopic endonasal transsphenoidal surgery using a skull model and eggs *Acta Neurochirurgica* **152** 1801–4
[24] Okuda T, Yamashita J, Fujita M, Yoshioka H, Tasaki T and Kato A 2014 The chicken egg and skull model of endoscopic endonasal transsphenoidal surgery improves trainee drilling skills *Acta Neurochirurgica* **156** 1403–7
[25] Engel D C, Ferrari A, Tasman A-J, Schmid R, Schindel R, Haile S R, Mariani L and Fournier J-Y 2015 A basic model for training of microscopic and endoscopic transsphenoidal pituitary surgery: the egghead *Acta Neurochirurgica* **157** 1771–7
[26] Wen G, Cong Z, Liu K, Tang C, Zhong C, Li L, Dai X and Ma C 2016 A practical 3D printed simulator for endoscopic endonasal transsphenoidal surgery to improve basic operational skills *Childs Nerv. Syst.* **32** 1109–16
[27] Ding C-Y, Yi X-H, Jiang C-Z, Xu H, Yan X-R, Zhang Y-L, Kang D-Z and Lin Z-Y 2019 Development and validation of a multi-color model using 3-dimensional printing technology for endoscopic endonasal surgical training *Am. J. Transl. Res.* **11** 1040–8
[28] Gallet P, Rebois J, Nguyen D-T, Jankowski R, Perez M and Rumeau C 2021 Simulation-based training in endoscopic endonasal surgery: assessment of the cyrano simulator *Eur. Ann. Otorhinolaryngol. Head Neck Dis.* **138** 29–34
[29] Bandari N, Dargahi J and Packirisamy M 2020 Tactile sensors for minimally invasive surgery: a review of the state-of-the-art, applications, and perspectives *IEEE Access* **8** 7682–708
[30] Bekeny J R, Swaney P J, Webster R J III, Russell P T and Weaver K D 2013 Forces applied at the skull base during transnasal endoscopic transsphenoidal pituitary tumor excision *J. Neurol. Surg. B* **74** 337–41
[31] Golahmadi A K, Khan D Z, Mylonas G P and Marcus H J 2021 Tool-tissue forces in surgery: a systematic review *Ann. Med. Surg.* **65** 102268
[32] UltiMaker n.d. UltiMaker PLA TDS (available at: https://support.makerbot.com/s/article/1667410781972) (Accessed 25 November 2024)
[33] UltiMaker n.d. UltiMaker TPU 95A TDS (available at: https://support.makerbot.com/s/article/1667410781018) (Accessed 25 November 2024)
[34] Santona G, Fapanni T, Fiorentino A, Doglietto F and Serpelloni M 2023 Preliminary study of a sensorized system for real-time feedback for arachnoid collapse during neurosurgical training *2023 IEEE Int. Workshop on Metrology for Industry 4.0 & IoT (Metroind4.0&iot)* pp 233–8